Earth and Planetary Science Letters 309 (2011) 280–290

Contents lists available at ScienceDirect

Earth and Planetary Science Letters

journal homepage: www.elsevier.com/locate/epsl

High-resolution $^{40}Ar/^{39}Ar$ chronostratigraphy of the post-caldera (<20 ka) volcanic activity at Pantelleria, Sicily Strait

Stéphane Scaillet [a,*], Silvio G. Rotolo [b,c], Sonia La Felice [b], Grazia Vita-Scaillet [a]

[a] Laboratoire des Sciences du Climat et de l'Environnement (LSCE), UMR 8212 CNRS-CEA-OVSQ, l'Orme des Merisier, 91191 Gif sur Yvette, France
[b] Dipartimento di Scienze della Terra e del Mare (DISTeM), Università di Palermo, Via Archirafi 36, 90123 Palermo, Italy
[c] Istituto Nazionale di Geofisica e Vulcanologia, Sezione di Palermo, Via U. La Malfa, 153, 90146 Palermo, Italy

ARTICLE INFO

Article history:
Received 3 March 2011
Received in revised form 7 July 2011
Accepted 11 July 2011
Available online 5 August 2011

Editor: R.W. Carlson

Keywords:
pantelleria
$^{40}Ar/^{39}Ar$
xenocrysts
excess ^{40}Ar
anorthoclase

ABSTRACT

The island of Pantelleria (Sicily Strait), the type locality for pantellerite, has been the locus of major caldera-forming eruptions that culminated, ca. 50 ka ago, in the formation of the Cinque Denti caldera produced by the Green Tuff eruption. The post-caldera silicic activity since that time has been mostly confined inside the caldera and consists of smaller-energy eruptions represented by more than twenty coalescing pantelleritic centers structurally controlled by resurgence and trapdoor faulting of the caldera floor. A high-resolution $^{40}Ar/^{39}Ar$ study was conducted on key units spanning the recent (post-20 ka) intracaldera activity to better characterize the present-day status (and forecast the short-term behavior of) the system based on the temporal evolution of the latest eruptions. The new $^{40}Ar/^{39}Ar$ data capture a long-term (>15 ka) decline in eruption frequency with a shift in eruptive pace from 3.5 ka^{-1} to 0.8 ka^{-1} associated with a prominent paleosol horizon marking the only recognizable volcanic stasis around 12–14 ka. This shift in extraction frequency occurs without major changes in eruptive style, and is paralleled by a subtle trend of decreasing melt differentiation index. We speculate that this decline probably occurred (i) without short-term variations in melt production/differentiation rate in a steady-state compositionally-zoned silicic reservoir progressively tapped deeper through the sequence, and (ii) that it was possibly modulated by outboard eustatic forcing due to the 140 m sea level rise over the past 21 ka. The intracaldera system is experiencing a protracted stasis since 7 ka. Coupled with recent geodetic evidence of deflation and subsidence of the caldera floor, the system appears today to be on a wane with no temporal evidence for a short-term silicic eruption.

1. Introduction

Silicic centers with high magma output commonly display cyclicity in their explosive activities that reflect a complex interplay between the evolution and storage of magmas in the shallow crust and the mechanisms triggering eruption at depth (density changes, volatile build-up, magma recharge, etc.). Recent (sub-active or dormant) silicic centers can offer well-preserved depositional sequences recording the temporal succession and overlap of such mechanisms. Precise and accurate dating of such sequences allows, in principle, quantification of the recurrence pattern of major eruptions and their magmatic triggers, providing critical information to petrogenetic models currently developed to predict the short-term behavior of active systems and implement strategies of hazard mitigation.

High-resolution $^{40}Ar/^{39}Ar$ studies have become increasingly effective at constraining the evolution of very youthful volcanic fields (e.g., Escobar-Wolf et al., 2010; Frey et al., 2004; Gamble et al., 2003; Harford et al., 2002; Heizler et. al, 1999; Hora et al., 2007; Jicha and Singer, 2006; Singer et al., 2008). This commonly requires particularly meticulous experimental procedures for accurate correction of the atmospheric contamination and samples displaying optimal K-content, ideally sanidine (Scaillet and Guillou, 2004). Another difficulty commonly associated with highly explosive systems is xenocrystic contamination resulting from syn-eruptive reworking of older crystals from pre-existing deposits (e.g., Gansecki et al., 1996; Scaillet et al., 2008; Spell et al., 2001), or from incorporation by partial assimilation/disaggregation of older xenoliths prior to eruption (e.g., Heizler et al., 1999). Mixing of juvenile and xenocrystic components with subtle age differences in the range 10^3–10^4 yr may pass undetected in old eruptive sequences (>500 ka) because these are swamped by the analytical uncertainties. In ultra-young sequences, inferring an accurate eruptive chronology in such circumstances may be problematic, especially if the $^{40}Ar/^{39}Ar$ resolution approaches the average repose time between consecutive eruptions.

In this study, we show how these technical and natural limitations affect the $^{40}Ar/^{39}Ar$ systematics of the most recent (post-20 ka) volcanic activity of the island of Pantelleria in the Strait of Sicily (Fig. 1), the youngest peralkaline center ever dated by this technique.

* Corresponding author. Tel.: +33 1 69087012; fax: +33 1 69087716.
E-mail address: scaillet@lsce.ipsl.fr (S. Scaillet).

0012-821X/$ – see front matter © 2011 Elsevier B.V. All rights reserved.
doi:10.1016/j.epsl.2011.07.009

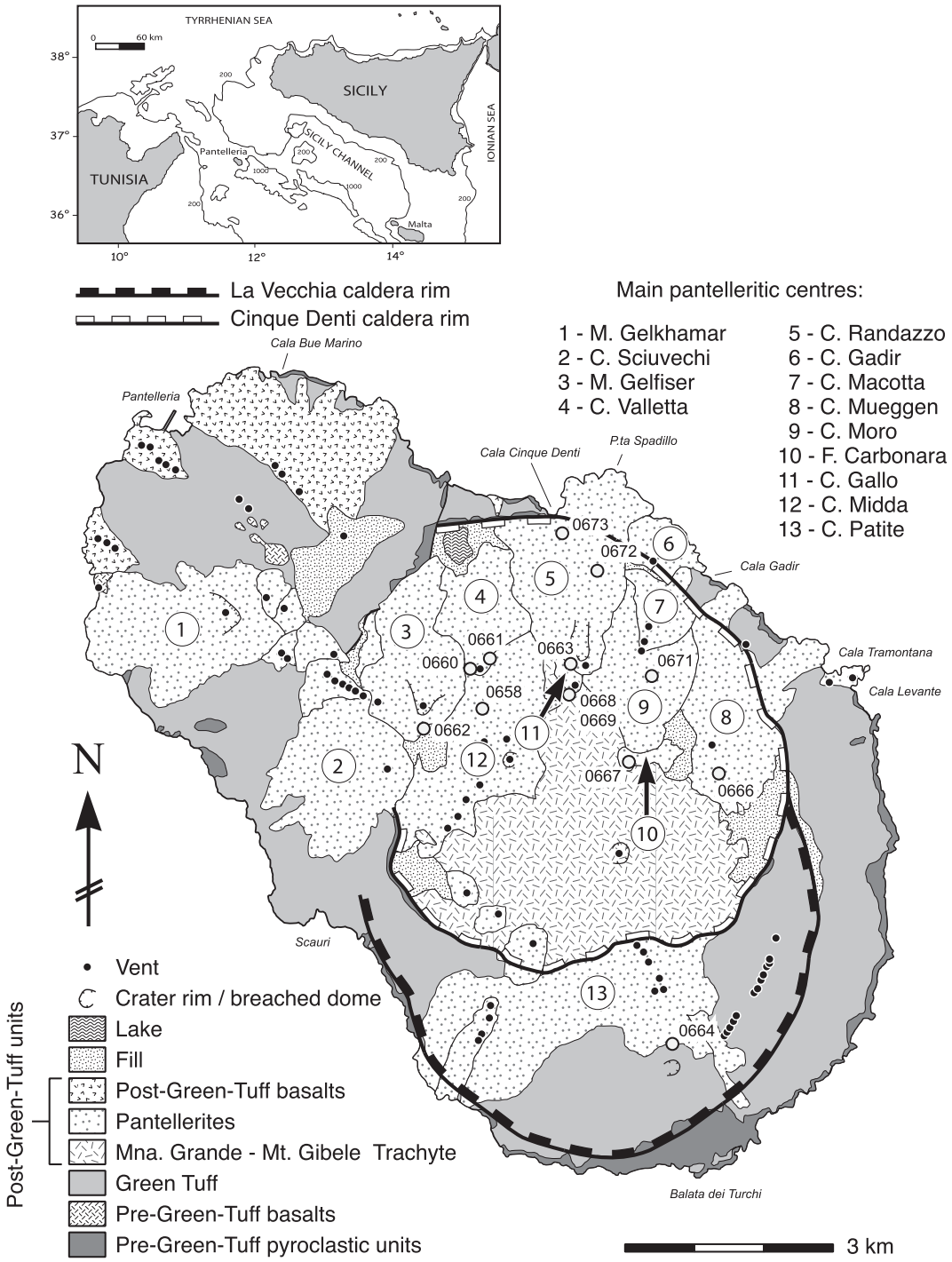

Fig. 1. Geological sketch map of Pantelleria with sample location (adapted from Mahood and Hildreth, 1986). Structural-morphological classification of post-caldera pantellerite units according to Mahood and Hildreth (1986): C. Valletta, C. Macotta, C. Mueggen = moat shields; C. Gadir, C. Patite, C. Sciuvechi, M. Gelfiser, C. Randazzo = rim shields; C. Mida, C. Gallo, F. Carbonara, Fossa del Russo, Monti Gibbili domes = trapdoor and hingeline vents; M. Gelkhamar = early extracaldera pantelleritic trachyte center. Small radial centers are unlabelled (C. Glindo, C. d'Almanza, C. San Vito, C. Bonsulton, Cuddioli di Contrada Caffefi, Punta Tracino, Valenza flows, C. Bellizzi). Small hingeline units sampled in this study but too small to be outlined are detailed in close-up map of Fig. S1.

$^{40}Ar/^{39}Ar$ dating at Pantelleria is challenging not only because of the youthfulness of the erupted products, but also due to the mildly enriched K-content of the target phase available for dating (anorthoclase, the K–Na solid-solution feldspar with K_2O wt.% = 5–6 versus 12 wt.% for pure sanidine). At a given atmospheric contamination level, a two-fold reduction in K content nominally results in a two-fold reduction of the resolving power of the $^{40}Ar/^{39}Ar$ technique for very young (<100 ka) samples (Scaillet, 2000). This imposes very stringent criteria of sample selection and *in vacuo* processing to achieve a similar age precision (on the order of a few centuries) as for sanidine. Here, we combine detailed field and petrologic information with $^{40}Ar/^{39}Ar$ laserprobe data to unravel fine-scale temporal relationships among recent intracaldera deposits previously interpreted as recording distinct silicic cycles. With a five-fold improvement in resolution relative to previous K–Ar work, the new $^{40}Ar/^{39}Ar$ ages reveal previously unsuspected short-term variations in eruptive pace that

we discuss in terms of internal (magmatic) vs. external (eustatic) control.

2. Previous geochronology and petrogenetic models

Pantelleria is the type locality of pantellerite, a strongly Fe-enriched peralkaline rhyolite (Washington, 1914). Volcanism has been active at Pantelleria since at least 520 ka (Rotolo and Villa, 2001) until the last AD 1891 submarine basaltic eruption 5 km NW off the island (Washington, 1909). The structure of Pantelleria is dominated by two nested calderas in the central part of the island (Fig. 1): (i) the "La Vecchia caldera", ~42 km^2, formed around 114 ka (Mahood and Hildreth, 1986); (ii) the younger "Cinque Denti caldera" (Mahood and Hildreth, 1986) or "Monastero caldera" (Cornette et al., 1983), ~30 km^2, that collapsed during the Plinian eruption of the Green Tuff (GT) ignimbrite, ca. 50 ka ago (Civetta et al., 1988; Mahood and Hildreth, 1986).

The recent (post-GT) activity mostly consists of resurgent felsic volcanism almost entirely confined inside the Cinque Denti caldera. Large volumes of trachytic magma (~3 km^3) initially outpoured between ca. 47–30 ka to form a large intracaldera shield (the Montagna Grande–Monte Gibele unit; Civetta et al., 1988; Mahood and Hildreth, 1986; Fig. 1). A trend towards more evolved magmas followed with the emission of progressively more peralkaline trachyte-pantellerite magmas, accompanied by trapdoor faulting and uplift of the intracaldera trachyte shield to form the summit of Mgna. Grande. The post-trachytic (<20 ka) volcanism, which is the focus of this study, produced as many as 24 silicic eruptive units represented by coalescing pantelleritic centers structurally and geomorphologically controlled by the intracaldera rim and trapdoor fault network (Hildreth and Mahood, 1986; Orsi et al., 1991; Fig. 1). Extracaldera basaltic volcanism occurred contemporaneously at 27 ka and <10 ka (Civetta et al., 1984, 1988) with extrusion and building of lava fields and cones in the North of the island along vents aligned NW–SE, parallel to the regional main rift axis (Fig. 1).

Two contrasting petrogenetic models have been proposed for the generation of post-GT peralkaline rhyolites at Pantelleria: (i) protracted fractional crystallization (FC) from an alkali basaltic source (Civetta et al., 1998; White et al., 2009), or (ii) a two-step process involving low-degree partial melting of a mafic and alkaline non-mantle source (cumulates) to form trachyte melts futher evolving by low-pressure FC to pantellerite (Avanzinelli et al., 2004; Lowenstern and Mahood, 1991; Mahood and Hildreth, 1986). Recent petrogenetic modeling confirmed the low temperature of crystal-melt equilibria of pantellerites and the need for extreme fractionation from a mantle source to produce pantellerite compositions (White et al., 2005, 2009). Integration of field and petrographic data led Mahood and Hildreth (1986) to suggest the existence of a low level magma chamber progressively evolving into a stratified reservoir by closed-system FC, incrementally producing volatile-enriched pantelleritic magmas atop a residual (metaluminous) trachyte melt left behind by the Mgna. Grande precursor. Based on a detailed structural–geomorphological analysis complemented by some K–Ar and ^{14}C ages, they classify the post-trachyte silicic activity as moat/rim shields, moat cones, trapdoor and hingeline vents, and radial centers structurally controlled by progressive inflation of the developing high-level differentiated reservoir during trapdoor uplift (Fig. 1).

In contrast, Cornette et al. (1983), Civetta et al. (1984, 1988, 1998), and Orsi et al. (1991) interpret the post-GT caldera activity as a piecewise succession of six silicic cycles with differentiation trends internal to each cycle for which they propose a mechanism of magma tapping from a zoned magma chamber episodically evolving by periodic recharge from a deep-seated magma source and subsequent maturation by closed-system differentiation. Their subdivision is based on grouping of total-fusion K–Ar ages from closely dated units, as well as on the occurrence of three incipient to well-developed paleosols between their Cycles III–IV, IV–V, and V–VI (Fig. 2). The greater analytical precision of their unspiked K–Ar data (on average ±2.5 ka at 2σ; cf. Table S1), nicely confirmed the space–time relationships inferred mostly geomorphologically by Mahood and Hildreth (1986), in particular regarding the younger age of trapdoor/hingeline vents relative to rim and moat centers, with the following correspondence: Cycle II [26–37 ka] = trachytic moat centers, Cycle III [19–24 ka] = radial and extracaldera pantelleritic vents, Cycle IV [14–20 ka] = moat and extracaldera centers, Cycle V [12–15 ka] = rim centers, and Cycle VI [10–5 ka] = hingeline vents. The volume and age of the products collectively erupted at each cycle were correlated by Civetta et al. (1988) with variations in melt differentiation index (monitored via the Zr concentration) to infer a time-predictive model of eruptive periodicity. Based on a steady-state extrusion rate of 0.1 km^3/ka averaged over the past 50 ka, their model predicts a forthcoming silicic eruption within ~2 ka.

3. Goals and $^{40}Ar/^{39}Ar$ working strategy

While previous K–Ar studies have been essential in working out a first detailed chronostratigraphy of the post-caldera activity, two major uncertainties remain.

(1) Whereas the first two cycles of Civetta et al. (1988) and Orsi et al. (1991) are well resolved by their K–Ar data, the subdivision of the last four appears questionable. Previous K–Ar data actually overlap continuously from about 22 ka down to 8 ka, without any gap in the age distribution to indicate temporally well-resolved breaks in effusive activity (Fig. 2). Obviously, establishing whether or not the post-caldera activity is pulsatory in behavior, and indeed driven by well-defined (predictable) cyclic pulses in differentiation/extrusion rate, is mandatory for a meaningful understanding of the current state of the plumbing system and a proper assessment of forthcoming hazards.

(2) One of the main difficulties faced by previous workers was the rather limited (by current standards) analytical resolution of earlier K–Ar determinations, with errors in excess of 2–4 ka. Another limitation not fully appreciated by previous studies (except by Mahood and Hildreth, 1986) was the problem of ^{40}Ar inheritance (in particular via xenocrystic contamination) that cannot be obviated by bulk-fusion K–Ar dating. Coupled

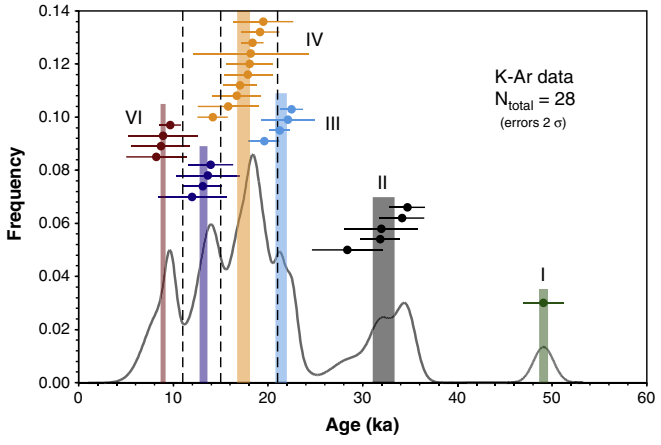

Fig. 2. Age-frequency chronogram of the post-Green Tuff volcanic activity based on prior K–Ar ages from Cornette et al. (1983), Civetta et al. (1988), and Orsi et al. (1991), and recalculated in this study (Table S1). Silicic-cycle subdivision from original authors is denoted by roman numerals (I to VI) next to defining K–Ar cluster (plotted with distinctive colors). Vertical colored strips represent mean weighted age of corresponding K–Ar cluster. Vertical dashed lines between Silicic Cycles III and IV, IV and V, and V–VI denote intervening paleosols inferred by Civetta et al. (1988) and Orsi et al. (1991).

Table 1
Representative whole rock XRF analyses of $^{40}Ar/^{39}Ar$ samples.

Location and rock type	Eruptive Unit, type/magnit.(1)	Sample #	U.T.M. coordinates	Altitude (m. a.s.l.)	Zr (ppm) (2)	Nb (ppm) (2)	P.I. (2)	Phenocrysts abundance and composition (3)
GALLO (agglutinate spatter)	GALLO Explosive (Stro.)	#69	33S0232765 4076446	424	1597	361	1.52	Kfs (Ab = 64, Or = 34, An = 2) > cpx (Hed, Agt) > enig > Fe–Ti ox > ol (Fa) > qtz
RANDAZZO (pumice)	RANDAZZO (Stro.)	#63	33S0232765 4077082	325	1570	351	1.47	Kfs (Ab = 67, Or = 33) > cpx (Hed, Agt) > ol (Fa) > enig > Fe–Ti ox > qtz
KHAGGIAR (lava)	RANDAZZO (lava flow)	#72	33S0233107 4078575	90	1767	397	1.65	Kfs (Ab = 63, Or = 37) > cpx (Hed, Agt) > ol (Fa) > enig > Fe–Ti ox > qtz
CASE								
SIRACUSA (pumice)	FASTUCA (sub-Plin.)	#58	32S0766755 4076175	372	1922	438	1.72	Kfs (Ab = 64, Or = 36) > enig > cpx (Hed, Agt) > amph > Fe–Ti ox > qtz
MUEGGEN (lava)	MUEGGEN (lava shield)	#66	33S0234675 4074875	196	2228	483	1.87	Kfs (Ab = 64, Or = 36) > enig > cpx (Agt)
PATITE (pumice)	PATITE (ultra-Stro.)	#64	33S0234062 4071615	406	2285	479	1.76	Kfs (Ab = 62, Or = 38) > enig > qtz > cpx (Agt)
GELFISER (lava)	GELFISER (lava shield)	#62	32S0766210 4076160	367	1992	441	1.71	Kfs (Ab = 65, Or = 35) > cpx (Agt) > enig > Fe–Ti ox > qtz
FOSSA								
CARBONARA (pumice)	CARBONARA (Stro.+ pyr. flow)	#67	33S0233591 4075447	377	2196	482	1.83	Kfs (Ab = 63, Or = 37) > cpx (Agt) > enig > Fe–Ti ox
RUNCUNI DI PIGNA (pumice)	RUNCUNI DI PIGNA (Stro.)	#71	33S0233934 4076930	257	2350	493	1.88	Kfs (Ab = 62, Or = 38) > cpx (Agt) > qtz > enig
GALLO	TIHIRRIKI (Stro.)	#68	33S0232765 4076446	424	2367	504	2.00	Kfs (Ab = 59, Or = 41) > enig > qtz
VALLETTA (lava)	VALLETTA (lava flow)	#60	32S0766602 4077000	278	2310	489	1.40	Kfs (Ab = 61, Or = 39) > cpx (Hd, Agt) > enig > qtz > Fe–Ti ox

All samples are pantelleritic in composition. (1) Eruptive Units and type/or magnitude of the given eruption (Stro. = strombolian; sub-Plin. = sub-Plinian; pyr.flow = pyroclastic flow), from Rotolo et al. (2007) and references therein. (2) Whole rock chemical data (X-Ray fluorescence), P.I. = whole rock peralkalinity index (= molar $(Na_2O + K_2O)/Al_2O_3$.). (3) Kfs = feldspar, (Ab = albite, An = anorthite, Or = orthoclase, mole%), Agt = aegirine–augite, Hd = hedembergite, enig = aenigmatite, amph = amphibole, Fa = fayalite, qtz = quartz, Fe–Ti ox = Ti-magnetite and/or ilmenite.

with the limited spatial extent and complex interfingered relationships of most post-trachyte units, this has obscured previous stratigraphic reconstructions, with important consequences in terms of petrogenetic modeling and inferred structural control on recent eruptions.

To better constrain the chronology of the most recent silicic activity, fourteen $^{40}Ar/^{39}Ar$ samples from ten key units were selected based on an extensive field-mapping and petrographic survey of the post-trachyte volcanism (Di Carlo et al., 2010; La Felice, 2008; Rotolo et al., 2007). These are mainly found on the northeastern sector of the young caldera (Fig. 1) and pertain to the "rim", "moat" and "trapdoor/hingeline" classification of Mahood and Hildreth (1986), and Cycles IV through VI of Civetta et al. (1988). Samples are listed along with their salient petrochemical characteristics, unit attribution, and GPS coordinates in Table 1 and are reported in Fig. 1. They consist of proximal fallout sequences of Strombolian type, one displaying a higher-magnitude ultra-Strombolian energy (Fastuca unit, Di Carlo et al., 2010), and a few subordinate lavas.

All samples are strongly peralkaline rhyolites, with a peralkalinity index P.I. = molar $(Na_2O + K_2O)/Al_2O_3$ ranging from 1.4 to 2.0 (Table 1). As is typical in pantellerites, Zr and Nb are very high (1245 to 2383 ppm and 350 to 512 ppm, respectively) and are positively correlated with the P.I (Table 1). All samples are porphyritic, with a phenocryst abundance (void-free, vol.%) ranging from ≤15 (pumices) to 25 (lavas). Anorthoclase (up to 2 mm in length) is the dominant phenocryst, followed by Na-hedenbergite and lesser amounts of enigmatite, ± fayalite, ± amphibole, ± Fe – Ti oxides, ± quartz (Table 1).

4. Analytical techniques

Laserprobe $^{40}Ar/^{39}Ar$ analyses were carried out at the LSCE on anorthoclase concentrates purified (>99%) by hand-picking under a binocular microscope. The freshness of the samples was checked on site by lens inspection and by thin-section examination in the laboratory, further complemented by bulk rock chemistry, mineral and glass compositional data and SEM imaging. Hand-picked crystals were cleaned with reagent-grade acetic acid in ultrasonic bath, then in acetone and finally washed in ultrapure ethanol. Traces of adhering glass were removed by etching in dilute (5%) hydrofluoric acid for 3 min in an ultrasonic bath. Some samples appeared more resistant to HF-etching, locally preserving tiny spots of thin residual glass coating their surface. Likewise, HF-etching was unable to eradicate melt inclusions (MI) trapped in grain interiors. The use of groundmass was deemed unsuitable for $^{40}Ar/^{39}Ar$ dating of lavas due to their frequent devitrification and widespread interaction with late-stage, saline-rich Cl-bearing fluids (Gioncada and Landi, 2010) susceptible to react more extensively with the groundmass relative to anorthoclase. Primary melt compositions are also characterized by high Cl concentrations (often up to 1 wt.%; Lowenstern, 1994), discouraging their use due to potential isobaric interferences on ^{38}Ar and ^{36}Ar.

$^{40}Ar/^{39}Ar$ analytical procedures and results are described in Supplemental files S1 and S3. ^{14}C data were obtained at the AMS facility housed at ARTEMIS (CEA, Saclay) and relevant technical details are provided in Supplemental file S2. Mineral analyses were performed at the University of Palermo on polished thin sections using a LEO™ 440 scanning electron microscope, coupled to an Oxford-Link EDS. Operating conditions were: 20 kV accelerating voltage and 600 pA beam current. Natural mineral standards were used for calibration. Whole-rock samples were analyzed for major and trace elements by X-ray fluorescence (XRF) on pressed powder pellets.

5. $^{40}Ar/^{39}Ar$ results

The laserprobe data are summarized and discussed in the form of probability density plots (Sircombe, 2004) illustrating the empirical

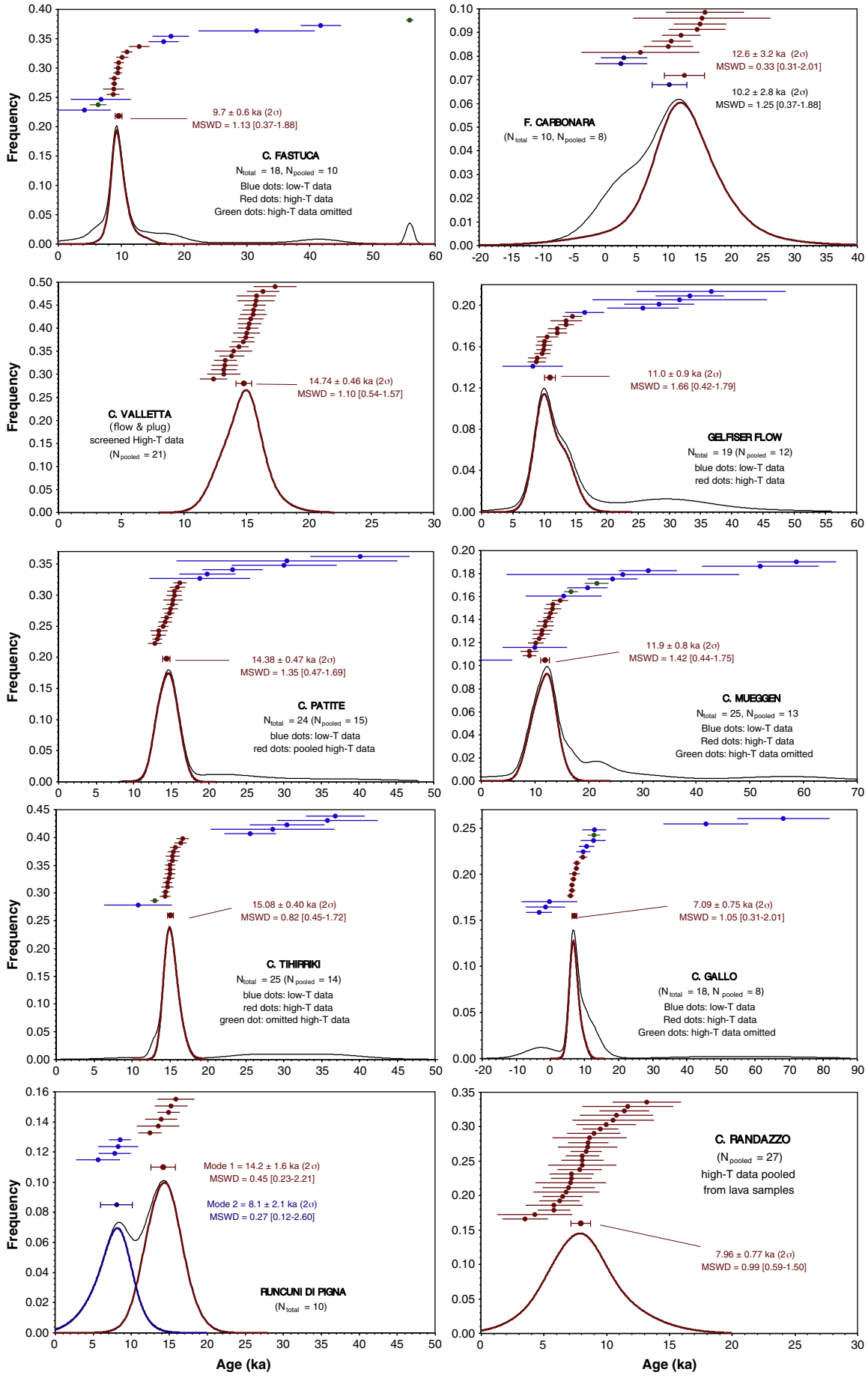
Frequency
9.7 ± 0.6 ka (2σ)
MSWD = 1.13 [0.37-1.88]
C. FASTUCA
N_total = 18, N_pooled = 10
Blue dots: low-T data
Red dots: high-T data
Green dots: high-T data omitted
12.6 ± 3.2 ka (2σ)
MSWD = 0.33 [0.31-2.01]
10.2 ± 2.8 ka (2σ)
MSWD = 1.25 [0.37-1.88]
F. CARBONARA
(N_total = 10, N_pooled = 8)
14.74 ± 0.46 ka (2σ)
MSWD = 1.10 [0.54-1.57]
C. VALLETTA
(flow & plug)
screened High-T data
(N_pooled = 21)
11.0 ± 0.9 ka (2σ)
MSWD = 1.66 [0.42-1.79]
GELFISER FLOW
N_total = 19 (N_pooled = 12)
blue dots: low-T data
red dots: high-T data
14.38 ± 0.47 ka (2σ)
MSWD = 1.35 [0.47-1.69]
C. PATITE
N_total = 24 (N_pooled = 15)
blue dots: low-T data
red dots: pooled high-T data
11.9 ± 0.8 ka (2σ)
MSWD = 1.42 [0.44-1.75]
C. MUEGGEN
N_total = 25, N_pooled = 13
Blue dots: low-T data
Red dots: high-T data
Green dots: high-T data omitted
15.08 ± 0.40 ka (2σ)
MSWD = 0.82 [0.45-1.72]
C. TIHIRIKI
N_total = 25 (N_pooled = 14)
blue dots: low-T data
red dots: high-T data
green dot: omitted high-T data
7.09 ± 0.75 ka (2σ)
MSWD = 1.05 [0.31-2.01]
C. GALLO
(N_total = 18, N_pooled = 8)
Blue dots: low-T data
Red dots: high-T data
Green dots: high-T data omitted
Mode 1 = 14.2 ± 1.6 ka (2σ)
MSWD = 0.45 [0.23-2.21]
Mode 2 = 8.1 ± 2.1 ka (2σ)
MSWD = 0.27 [0.12-2.60]
RUNCUNI DI PIGNA
(N_total = 10)
C. RANDAZZO
(N_pooled = 27)
high-T data pooled
from lava samples
7.96 ± 0.77 ka (2σ)
MSWD = 0.99 [0.59-1.50]
Age (ka)
Age (ka)

age distribution obtained for each sample (Fig. 3). All (but one, Runcuni di Pigna) units produced similar age patterns and $^{40}Ar/^{39}Ar$ systematics, so we discuss the data collectively in this section. The reader is referred to Supplemental file S3 for an extensive description of the stratigraphic relationships, petrography, and corresponding $^{40}Ar/^{39}Ar$ details for each separate unit. For reasons detailed in the Supplemental file S1, anorthoclase crystals were analyzed in clusters of 5–25 grains via two consecutive steps (low-T then high-T fusion step). Although the risk of incorporating xenocrysts cannot be excluded by this approach, the probability of resampling exactly the same proportion of xenocrysts is small at such low sampling levels under $N=25$ crystals, thereby minimizing the risk of producing homogeneously biased subpopulations as in bulk K–Ar dating involving as much as 2–8 g of aliquot. Accordingly, the occurrence of xenocrysts is expected to unambiguously show up as multi-modal distributions, providing a robust test to discard suspiciously older and erratic ages. The two-step degassing procedure was applied to enhance both the radiogenic yield and the age precision of the fusion step. The initial low-T steps systematically resulted in highly-contaminated, low-resolution ($2\sigma \geq 5$ ka) ages generally in excess of the ensuing fusion step. These data generally produce a coarse tail flanking a dominant mode typically formed by the high-T data (Fig. 3). (Note that not all samples were analyzed for the low-T fraction due to its low age-constraining power, as well as to avoid degrading the analytical conditions for the subsequent high-T step.)

Our $^{40}Ar/^{39}Ar$ analysis is based on screening out the low-T steps to retrieve a well-defined unimodal plot characteristic of homogeneous (i.e. isochronous) crystal populations for which a maximum-likelihood age estimate can be derived by calculating the inverse-variance weighted mean of the selected data populating the mode (Sambridge and Compston, 1994). The corresponding uncertainty is computed as the inverse square root of the sum of the weights and is reported at $\pm 2\sigma$ (95.4% C.L.). As a test of internal consistency, a sum of squared weighted residuals (S) is computed for each screened high-T mode, assuming all scatter is due to analytical errors alone. Although S is χ^2-distributed with an expectation converging to $N-1$ for large-sample statistics (e.g., Press et al., 1992), the distribution is increasingly asymetric for smaller degrees of freedom when $N<20$ (Wendt and Carl, 1991). Accordingly, to judge whether under- or excess-scatter is present, we resort to tailored upper and lower cutoff values to rigorously derive a fiducial interval for the normalized scatter index $MSWD = S/(N-1)$ (where N = number of data included in the mode; see Brooks et al., 1972). These bounds are retrieved at the 95% C.L. by computing the inverse of the χ^2 density distribution for $N-1$ degrees of freedom at the level of risk $\alpha = 0.025$ and $\alpha = 0.975$, respectively (cf. Scaillet and Guillou, 2004).

Except for the bimodal sample of Runcuni di Pigna, all high-T modes showed a high degree of internal consistency manifested by *MSWD*-statistics falling in the corresponding fiducial interval (Fig. 3). For some samples, the dominant mode was retrieved after discarding a few outlying high-T ages in addition to the low-T component (Valletta, Mueggen, Fastuca, Gallo Units, Fig. 3). As discussed later, these outliers are argued to represent accidental xenocrystics. Preferred ages inferred from maximum probability density analysis (MPDA) and field relationships (cf. Supplemental file S3) are summarized for each unit in Table 2 along with isochron parameters derived from the corresponding data. Three-isotope inverse correlation plots generally yield isochron parameters consistent with the mode derived from MPDA, with a trapped $^{40}Ar/^{36}Ar$ component concordant (in all but three cases, Valletta, Randazzo, and Gallo Units) with the atmospheric ratio of 295.5 (Fig. S2). Details of the isochron analysis are given in Supplemental file S3. Isochron ages are in general less precise than the corresponding MPDA mode due to propagation of uncertainties in the trapped $^{40}Ar/^{36}Ar$ (adjusted as a free parameter). Because isochron ages are not statistically different from – or fall very close to – the MPDA estimates (including those affected by non-atmospheric intercepts), the latter are preferred.

6. Discussion

The chronogram of the volcanic activity derived from the new $^{40}Ar/^{39}Ar$ data is displayed in Fig. 4. In this plot (bottom diagram), MPDA $^{40}Ar/^{39}Ar$ estimates are ordered by increasing stratigraphic age in the first place, then by apparent $^{40}Ar/^{39}Ar$ age when direct field relationships are lacking. The consistency between the $^{40}Ar/^{39}Ar$ age estimates and the stratigraphic relationships is illustrated by the monotonous age progression of the individual data along the temporal axis. Such a coherence is particularly rewarding given the difficulty of dating such youthful rocks and the moderately enriched K-content of anorthoclase, providing an external cross-check important to validate the $^{40}Ar/^{39}Ar$ ages. With a three- to five-fold improvement in analytical precision (on average ± 0.7 ka, 2σ), the $^{40}Ar/^{39}Ar$ data substantially improve the temporal framework of the post-caldera activity relative to previous K–Ar and paleomagnetic studies (Speranza et al., 2010). This is illustrated by the sharply defined peaks in eruptive frequency (bottom diagram, Fig. 4) relative to the smooth, bumpy curve derived from prior K–Ar data over the same interval (compare with Fig. 2). Overall, the $^{40}Ar/^{39}Ar$ ages are much more grouped than earlier K–Ar determinations for the same units. This is particularly true of three units previously ascribed to pre-Cycle IV eruptives (Gelfiser, Mueggen, and Patite units) that end up now much more tightly grouped between 16 and 7 ka relative to their previous K–Ar time range (i.e., 24–7 ka).

The newly established $^{40}Ar/^{39}Ar$ chronostratigraphy bears on several issues regarding (i) the significance of excess argon and xenocrystic contamination for such youthful products, (ii) their consequences for the eruptive cyclicity alleged from prior K–Ar data, and (iii) the implications in terms of integrated volcanic throughput and magma productivity over the past 20 ka. We discuss these in turn below.

6.1. Excess argon systematics vs. xenocrystic contamination

The dominant age unimodality observed for all (but one) samples argues against significant contribution from excess argon in the screened high-T data. Yet, anomalously high apparent ages do systematically appear in low- and (sometimes) high-T data (Fig. 3). At Pantelleria, ubiquitous evidence of interaction with hypersaline fluids (with halite expressed as an index phase; e.g. Fastuca unit; Rotolo et al., 2007) and/or hypersaline immiscible melts (Lowenstern, 1994), along with ongoing geothermal activity (Chierici et al., 1995), all provide natural candidates to explain such a contamination. Also, although the hand-picking procedure tried to avoid crystals crowded by MI's, completely MI-free crystals are rare and the estimated MI concentration in the final concentrates is ca. 1–5 vol.%, with a fairly homogeneous MI distribution among subsamples of a given population. Because pantellerite melts are Cl-rich (up to 1 wt.%), the corresponding bulk nominal wt.% Cl occluded in anorthoclase ranges between 0.01 and 0.05 (or $Cl/K \approx 10^{-2}$–10^{-3}), making a strong case for expecting a distinctly enriched $^{38}Ar_{Cl}$ signature if MI's were to decrepitate/melt and degas some unsupported ^{40}Ar at low- and/or high-T (see Esser et al., 1999).

Fig. 3. $^{40}Ar/^{39}Ar$ frequency density plots of anorthoclase clusters from post-20 ka intracaldera units at Pantelleria. Data in red (dots and curves) refer to selected high-T data as explained in text. Blue dots refer to screened low-T data. Green dots denote accidental high-T outliers omitted from dominant mode calculations. Individual ages are $\pm 1\sigma$ while pooled mode ages are $\pm 2\sigma$. *MSWD* refers to scatter statistics with corresponding 95% C.L. fiducial interval in square brackets as discussed in text.

Table 2
Summary of $^{40}Ar/^{39}Ar$ data and isochron parameters for all dated units in this study.

Unit	Sample field number	Facies	MPDA age (ka ± 2σ)	MSWD = S/(n−1) [95% F.I.]	*n*/N	Total age (ka ± 2σ)	Highest low-T age	Highest high-T age	Isochron age (ka ± 2σ)	MSWD	*n*/N	($^{40}Ar/^{36}Ar$) trapped (±2σ)
C. Gallo	#69	Pumice	7.1 ± 0.8	1.05 [0.31−2.01]	8/18	8.2 ± 0.8	68 ± 26	13 ± 4	9.0 ± 1.7	1.2	12/18	291.8 ± 2.8
C. Randazzo	#63	Pumice cone	NA	NA	NA	12.3 ± 1.8	89 ± 32	21 ± 4	NA	NA	NA	NA
″	#72	Lava	7.7 ± 1.8	0.79 [0.27−2.10]	7/13	11.9 ± 5.0	42 ± 60	12 ± 8	6.3 ± 6.9	0.86	13/13	299.2 ± 8.6
″	#73	Lava	8.0 ± 1.0	0.64 [0.37−1.88]	10/20	9.0 ± 1.0	50 ± 40	16 ± 4	8.0 ± 1.8	0.89	19/20	295.7 ± 2.6
″	PAN-23	Enclave	7.8 ± 1.4	1.60 [0.37−1.88]	10/10	7.8 ± 1.4	NA	13 ± 6	4.3 ± 5.5	1.08	10/10	300.0 ± 3.6
″	Pooled	Pooled	8.0 ± 0.8	0.99 [0.59−1.50]	27/45	8.7 ± 0.8	NA	13 ± 6	6.1 ± 1.2	1.1	39/41	298.9 ± 1.6
S. Fastuca	#58	Pumice	9.7 ± 0.6	1.13 [0.37−1.88]	10/18	16.7 ± 1.5	42 ± 6	56 ± 2	9.4 ± 1.3	1.6	13/18	295.7 ± 10
Gelfiser	#62	Lava plug	11.0 ± 0.9	1.66 [0.42−1.79]	12/19	11.0 ± 0.9	37 ± 24	15 ± 4	10.9 ± 3.7	1.8	14/19	295.0 ± 6.8
C. Mueggen	#66	Lava	11.9 ± 0.8	1.42 [0.44−1.75]	13/25	12.9 ± 0.8	102 ± 48	22 ± 4	11.8 ± 2.1	1.6	18/25	295.6 ± 3.6
Fossa Carbonara	#67	Pumice	12.6 ± 3.2	0.33 [0.31−2.01]	8/10	10.2 ± 3.0	NA	16 ± 12	4.5 ± 1.8	1.3	10/10	298.8 ± 7.4
Runcuni di Pigna	#71	Agglutinate	14.3 ± 1.7	0.45 [0.23−2.21]	6/10	12.2 ± 1.3	NA	16 ± 4	14.2 ± 4.1	0.58	6/10	295.5 ± 7.2
C. Patite	#64	Pumice	14.4 ± 0.5	1.35 [0.47−1.69]	15/24	15.8 ± 0.5	540 ± 130	76 ± 4	13.9 ± 1.0	1.2	17/24	298.6 ± 4.6
Tihirriki	#68	Pumice	15.1 ± 0.4	0.82 [0.45−1.72]	14/25	14.9 ± 0.4	160 ± 20	17 ± 2	15.0 ± 0.6	0.85	14/25	297.5 ± 6.4
C. Valletta	#60		14.8 ± 0.7	0.88 [0.37−1.88]	10/18 11/18	15.4 ± 0.6	34 ± 18	23 ± 4	13.3 ± 1.1	1.2	15/18	305.7 ± 3.6
″	#61	Lava	14.7 ± 0.6	1.40 [0.39−1.83]	11/18	15.0 ± 0.6	54 ± 28	20 ± 4	14.6 ± 2.1	1.3	15/18	295.5 ± 7.4
″	Pooled	Pooled	14.7 ± 0.5	1.10 [0.54−1.57]	21/36	15.2 ± 0.4	54 ± 28	23 ± 4	13.2 ± 1.3	1.6	30/36	303.2 ± 4.2

MSWD: normalized scatter index [95% fiducial interval in square brackets].
S: sum of squared weighted deviates.
MPDA age: maximum probability density age.
n/N: selected/total number of fractions.
NA: non-applicable.

Actually, the $^{38}Ar_{Cl}$ did not show high concentration levels systematically correlated either with the low-T ages or MI abundance (Table S2). The lack of apparent $^{38}Ar_{Cl}$ signature cannot be used, however, to rule out the effects of chlorine and MI altogether. Cd-shielding was used to suppress $^{40}Ar_K$ interference from thermal neutrons. This lowered the net yield of $^{38}Ar_{Cl}$ from thermal neutron capture on chlorine by a factor of 100, resulting in a net $^{38}Ar_{Cl}/^{39}Ar_K$ ratio (from the highest nominal $Cl/K \approx 10^{-2}$) at best 15 times lower than the production factor of $^{38}Ar_K$ from potassium. Simply stated: the highest possible $^{38}Ar_{Cl}/^{39}Ar_K$ ratio here amounts to just a small fraction (~7%) of the $[^{38}Ar/^{39}Ar]_K$ correction factor and is correspondingly swamped by the associated error. In fact, most measured $^{38}Ar_{Cl}/^{39}Ar_K$ ratios lie below 10^{-4} or within error of zero, with rare tiny spikes showing up in the low-T data (Table S2). Thus, although the anomalously older ages in the low-T steps might well reflect contamination with surface- or impurity-bound excess ^{40}Ar associated with Cl (e.g., residual adhering glass, or low-T decrepitating late-stage fluid inclusions), irradiation conditions prohibit a more quantitative assessment of this component.

The excess scatter in high-T ages of some samples (e.g., Valletta, Mueggen, Fastuca, Gallo Units, Fig. 3) cannot be equated with variations in MI concentration, even though the latter cannot be traced via $^{38}Ar_{Cl}$. Indeed, MI's are homogeneously distributed among grains within a given sample subpopulation while the excess ages are random. This suggests that these high-T data do not reflect contribution from excess-bearing MI's but true xenocrystic contamination. This contamination is accidental though not uncommon (Fig. 3). The most informative example comes from Randazzo unit for which we sampled in detail the pumice and lava facies (cf. Supplemental file S3). Isotopically, the pumice cone of this unit is the most severely xenocryst-corrupted sample of this study with only a single high-T age consistent with the inferred age of eruption (8 ka, Table 2, as derived from the companion facies). We initially correlated this behavior with the unusually high abundance, in this facies, of trachytic enclaves displaying large sanidine crystals that could be accidentally admixed with anorthoclase into the final separates (cf. Supplemental file S3). Some of these enclaves potentially derive from reworked trachyte xenoliths scavenged from the nearby Mgna. Grande – M. Gibele trachyte shield (K–Ar = 28 ± 16 to 44 ± 8 ka, Mahood and Hildreth, 1986).

As discussed in detail in Supplemental file S3, separate analysis of one such trachytic enclave actually shows its alkali feldspars to be completely equilibrated with an atmosphere-like component and the age of the deposit at 8 ka. That they are not carriers for any inherited excess ^{40}Ar is further supported by the data from the companion lava facies (sample #72) also carrying abundant trachytic enclaves but lacking any contamination by older high-T ages (Table S2). Based on available evidence, we infer that alkali feldspars from admixed/disaggregated enclaves are not the cause for xenocrystic contamination in this and other units. This is corroborated by (i) the explosive Gallo pumice unit which shows only one anomalously old high-T age (Fig. 3) in spite of equally abundant trachytic enclaves, and (ii) the Gelfiser lava sample that lacks apparent high-T outliers despite very abundant trachytic enclaves embedded in the flow (Fig. 3). Such enclaves commonly exhibit contorted/lobate surfaces, suggesting extensive interaction at high-T along with residence times sufficient to erase any precursor ^{40}Ar (e.g., Heizler et al., 1999). Survival of pre-eruptive

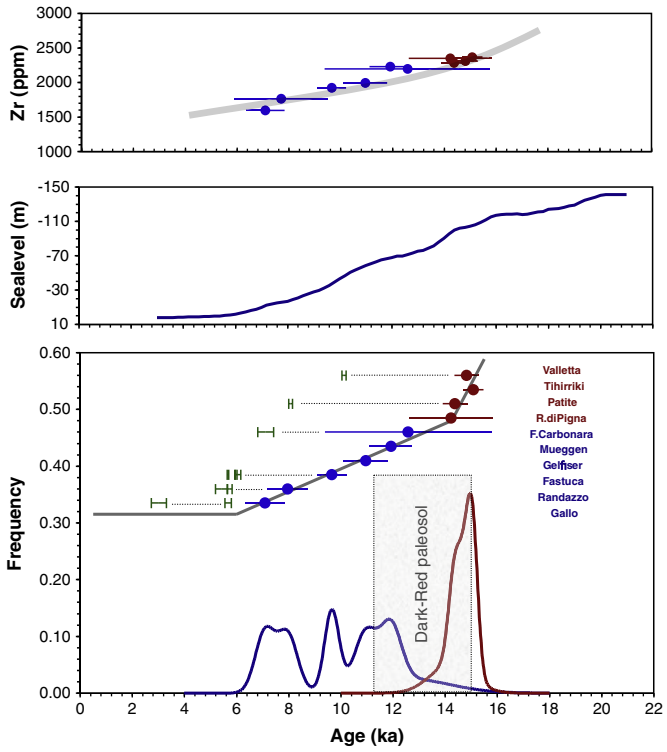

Fig. 4. Chronogram of volcanic activity of post-caldera pantellerites from $^{40}Ar/^{39}Ar$ ages determined in this study. Lower plot: individual $^{40}Ar/^{39}Ar$ ages ($\pm 2\sigma$, blue and red dots) arranged in stratigraphic order from Gallo Unit (younger) to Valletta Unit (older). Blue and red colors are used to highlight pre- and post-DRP deposits. Vertical shaded box displays duration of formation of the dark-red paleosol inferred from bracketing deposits. Green symbols: 95% C.L. ^{14}C age-interval of corresponding units (from this study, Mahood and Hildreth, 1986; and Civetta et al., 1988, 1998). Note systematic bias between $^{40}Ar/^{39}Ar$ and ^{14}C ages. Straight-line best fits through the $^{40}Ar/^{39}Ar$ data arrays yield the corresponding mean eruption frequency with a marked kink at ca. 14 ka. Upper plots: global sea level variation for the past 20 ka (from Lambeck and Chappel, 2001) and differentiation index trend monitored via Zr.

high-T ages thus most likely reflects accidental (vent-specific) admixing processes with older near-surface deposits.

In conclusion, two potential sources for excess ^{40}Ar are identified in post-20 ka eruptives at Pantelleria. (i) One released at low-T and possibly involving late-stage Cl-bearing fluids related to exsolved immiscible hypersaline solutions or hydrosaline melts. (ii) The second carried by true accidental xenocrysts derived from near-surface reworking of older deposits rather than from older (trachyte) high-T enclaves. Noteworthy, although MI's are ubiquitous in almost all anorthoclases studied, these occur decoupled from any systematic excess ^{40}Ar signature. We infer that, unlike late-stage exsolved fluids, trapped primary melts in anorthoclases sampled here are largely free of extraneous ^{40}Ar. Unlike the extensively excess-corrupted MI-rich anorthoclases from Mt. Erebus (Esser et al., 1999), anorthoclase crystals at Pantelleria retain geologically meaningful high-T ages reflecting their timing of eruption (juvenile component) or a vestige of their precursor component (xenocrysts).

6.2. Eruptive cyclicity: comparison with previous K–Ar data and evidence from paleosols

The occurrence of xenocrysts and low-T excess ^{40}Ar contamination represents two potential complications that may have flawed prior chronostratigraphic reconstructions based on K–Ar ages alone. In the light of such evidence, we re-examined in detail the original K–Ar data of Civetta et al. (1988) and Orsi et al. (1991) to check the extent to which these conform with the formal assumption of trapped amospheric argon inherent to K–Ar ages (i.e.: $(^{40}Ar/^{36}Ar)_{trapped} = 295.5$). Although this information is not contained in the original data, a simple test of internal consistency was undertaken by extrapolating a 2-point pseudo-isochron for each paired K–Ar replicate, or by computing standard isochron parameters for K–Ar samples with $N>2$.

Fourteen out of 29 K–Ar samples (Table S1) displayed sufficient spread in their data distribution with well-defined intercept values to make this approach informative. The corresponding pseudo-isochron ages are plotted against the relevant conventional K–Ar age in Fig. 5. Eight samples fall within error bars on the 1:1 line, suggesting that the assumption of atmospheric contamination holds for these K–Ar samples. In contrast, six clearly deviate from ideal behavior, giving pseudo-isochron ages on average 4 ± 2 ka younger than the conventional K–Ar age (C. Mueggen, C. Sciuvechi, P. Tracino, Le Carrucate, P. dell'Alca units), signaling most probably the presence of excess or xenocrystic ^{40}Ar. This difference gauges the bias potentially incurred by earlier K–Ar estimates due to excess/xenocrystic contamination and suggests that the effect may extend well beyond the present $^{40}Ar/^{39}Ar$ dataset. Such a bias exceeds the nominal uncertainty of K–Ar ages (~2 ka; see also Supplemental file S4), preventing resolution of distinct pulses or volcanic phases lasting (or separated by) less than about 4 ka by this technique. This is not to imply that all previous K–Ar ages are flawed by extraneous ^{40}Ar. Of the six K–Ar ages revisited in this study, two are conformal with the $^{40}Ar/^{39}Ar$ estimate (Randazzo and Tihirriki units), but the remaining four clearly show that the accuracy of prior K–Ar data cannot be assessed in the absence of independent $^{40}Ar/^{39}Ar$ control. This is especially true for pre-Cycle IV eruptives which have not been checked yet by $^{40}Ar/^{39}Ar$ (Fig. 2).

Another argument put forth by Orsi et al. (1991) and Civetta et al. (1988) in support of their model of silicic cycles was the occurrence of three paleosols between Cycles III–IV, IV–V, and V–VI (Fig. 2). The youngest one is the so-called dark-red paleosol (DRP), also recognized by Mahood and Hildreth (1986) on top of C. Valletta, C. Tihirriki, R. di Pigna units (see sample description and Supplemental file S3). The other two should be very incipient as they could not be identified despite extensive fieldwork during this study. Our data and field observations actually suggest that the paleosol purportedly separating Cycles III and IV at ca. 21 ka may be an unrecognized lateral equivalent of the DRP. Such a paleosol is described to occur underneath pumices from Gelfiser unit ($^{40}Ar/^{39}Ar = 11.0 \pm 0.9$ ka) and on top of effusives collectively lumped in Cycle III with C. Patite unit ($^{40}Ar/^{39}Ar = 14.4 \pm 0.5$ ka). Because field descriptions are lacking, it is unsure whether it

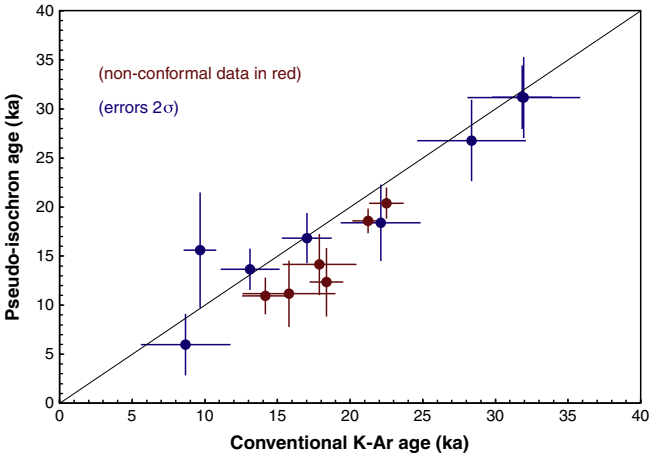

Fig. 5. Conventional versus pseudo-isochron age plot of selected (and recalculated) K–Ar data from Civetta et al. (1988) as listed in Table S1. Errors plotted are $\pm 2\sigma$. Non conformal data affected by excess ^{40}Ar (in red) plot below the 1:1 line.

occurs atop C. Patite proper, or on one of the other two units of Cycle III characterized by complex (scattered or excess-bearing) K–Ar systematics (Table S1). Taking at face value our $^{40}Ar/^{39}Ar$ brackets, we infer that this paleosol may represent a lateral equivalent of the younger DRP recognized elsewhere between Cycles V and VI.

The DRP is a locally thick (>1 m) and prominent alteration horizon in other respects more suggestive of a break in volcanic activity. The DRP was constrained by prior K–Ar data to occur between ca. 12 and 9 ka (Orsi et al., 1991). The tightest bracketing provided by our $^{40}Ar/^{39}Ar$ data is that derived from the underlying C. Valletta (14.7 ± 0.5 ka) and overlying Mueggen (11.9 ± 0.8 ka) units. These endpoints define a maximum stasis duration of 2.8 ± 0.9 ka centered at 13.3 ka (Fig. 4), significantly older and more tightly constrained than before. Importantly, re-allocation of Mueggen unit from Cycle IV [14–20 ka] to a more recent $^{40}Ar/^{39}Ar$ age of 12 ka independently agrees with its (previously unrecognized) occurrence above the DRP (cf. Supplemental file S3), emphasizing the uncertainties associated with earlier K–Ar determinations. A third paleosol was claimed to occur between Cycles IV and V (Fig. 2) atop C. del Moro (17.0 ± 1.7 ka; K–Ar, Table S1) and below Tihirriki unit (15.1 ± 0.4 ka; $^{40}Ar/^{39}Ar$, Table 2). Taking the K–Ar bracket as a maximum upper bound unscathed by excess ^{40}Ar would place this horizon around 16 ka within a short stasis spanning 1.9 ± 1.7 ka, probably explaining its faint development and problematic identification.

Taken as a whole, the paleosol record does not appear to substantiate the occurrence of more than one significant volcanic stasis throughout the 16–7 ka time span. Coupled with the $^{40}Ar/^{39}Ar$ evidence for excess argon, this further calls into question the cycle subdivision of Civetta et al. (1988) and Orsi et al. (1991), at least for the most recent intracaldera activity. Clearly, more $^{40}Ar/^{39}Ar$ work is needed before fine-scale (2–4 ka) changes in eruptive periodicity and melt production rates can be confidently resolved throughout the post-GT history.

Noteworthy, our $^{40}Ar/^{39}Ar$ ages are systematically older than the ^{14}C ages measured on charcoal incorporated in (or buried by) the fallout deposits (Fig. 4), a bias already noted by Civetta et al. (1988) between their K–Ar data and previously published ^{14}C ages (Civetta et al., 1998; Mahood and Hildreth, 1986). The greatest bias (4 ka) here is for the Fastuca fallout (9.7 ± 0.6 ka vs. 5.99–5.67 cal ka BP; Fig. 3 and Table 3) for which the effects of xenocystic and excess contamination were successfully resolved and, therefore, cannot be called upon to explain the discordance. Because high-T excess ^{40}Ar is accidental (cf. Section 6.1), it neither can provide a viable explanation for the systematic $^{40}Ar/^{39}Ar$ vs. ^{14}C age discordance observed for the complete suite as this would require ^{40}Ar excess contamination in such a way as to preserve the temporal succession implied by stratigraphic relationships. The radiocarbon data themselves produce mutually discordant ages among samples supposed to date the same eruption, in this as well as previous work (cf. Fig. 4). A systematic $^{40}Ar/^{39}Ar$ vs. ^{14}C bias has been similarly documented in other equally young pyroclastic sequences (Alban Hills: Giaccio et al., 2009; Vesuvius: Scaillet et al., unpublished data), suggesting that unsealed paleosols (or charcoal samples) capped by highly permeable pyroclastic deposits (or included in the deposit proper) can remain open to contamination with younger/modern carbon to produce spuriously young ^{14}C ages.

6.3. Eruptive pace and throughput: volcanic decline or eustatic forcing?

A salient feature emerging from the chronogram (Fig. 4) is the sharp and prominent mode produced at ca. 15 ka by the units stratigraphically older than the DRP, and the more distributed pattern produced by post-DRP units over 5 ka from 12 to 7 ka. Eruption rates derived from the pre- and post-DRP trends are 3.5 ka^{-1} and 0.8 ka^{-1}, respectively (materialized by the linear best fits through the data points). The break-in-slope hinging around 14 ka represents a four-fold decrease in aerial volcanic activity. The coincidence of the shift in eruptive pace with the volcanic stasis materialized by the DRP is probably not coincidental and signals a major change in the extraction and/or differentiation processes at the level of the magma chamber.

This overall decline in eruptive frequency could reflect a stepwise decrease in melt production rate in the silicic reservoir over the past 15 ka. However, the trend is not correlated with a reduction, nor a stepwise progression, in volumes erupted. Several units poured out rather similar volumes of lava flows and pumice ejecta early, in the middle, and near the end of the sequence (respectively: C. Patite, C. Mueggen, and C. Randazzo units), along with intervening episodes of small-sized (F. Carbonara unit) or higher-energy eruptions (Fastuca unit), a fact that does not argue for a purely magmatic origin of the progressive slowdown in throughput frequency. Erupted volumes are only very qualitatively constrained as yet, due to the complex interfingering relationships between recent deposits and the lack of detailed isopach mapping (Civetta et al., 1984; Orsi et al., 1991). Pending a more careful quantification, a precise mass budget may allow further refinement of magma productivity rates based on the newly established $^{40}Ar/^{39}Ar$ chronostratigraphy.

Petrographically, the prevailing picture is that of a persistent silicic reservoir that has been very regularly tapped throughout the last 16 ka with no major (nor consistent) changes in eruptive style and volatile content (Rotolo et al., 2007). A subtle but significant trend towards progressively less evolved magmas does exist, the youngest unit being the least evolved (e.g. C. Randazzo and C. Gallo units, P.I. = 1.6–1.5, vs. P.I. = 1.8 for C. Patite), a trend mirrored by the progressive decrease in Zr content throughout the sequence (Fig. 4). The progressively depressed eruptive pace is antipathetic to shorter residence times actually required to produce progressively less evolved magmas through the sequence, suggesting that, to the first order, throughput rates are largely decoupled from differentiation rates. The temporal–compositional trend rather suggests tapping of magma progressively deeper into a steady-state compositionally zoned reservoir (Rotolo et al., 2007).

The DRP development at ca. 13 ka occurred during a major climatic shift leading to the Holocene warming. That this change coincided both with a stasis in aerial volcanism and a four-fold reduction in eruptive pace suggests that both effects may be somehow related. A very suggestive climate-volcanic connection was previously explored by Wallmann et al. (1988) who showed that eustatic sea level changes could act as a trigger for eruption at Pantelleria by tensile stress accumulation and dyke propagation on top of a very shallow magma chamber due to sea level drop (and elastic pressure release) during glaciation. The reverse scenario may be envisioned whereby the sea level rise during warm interstadials would restore pre-glacial lithostatic stresses, thereby inhibiting eruption via dyke nucleation or fracture reactivation during interstadials. 140 m of sea level rise

Table 3
AMS radiocarbon data obtained on charcoal buried below fallout deposit or included in the pumice fall proper of Fastuca unit. pMC: percent modern carbon normalized to $\delta^{13}C = 25‰$. Age interval calibrated using INTCAL 04 and online calibration software (Oxcal at: http://www.rlaha.ox.ac.uk/O/oxcal.php).

ARTEMIS Lab #	Sample #	Unit	Facies	C (mg)	$^{13}C‰$	^{14}C activity (pMC)	^{14}C age BP	Calibrated age (ka)
#A 8152	#C-59	Fastuca	Charcoal–soil	0.74	−23.1	47.45 ± 0.19	5990 ± 30	5.99 ± 0.03
#A 8154	#C-69	Fastuca	Charcoal–airfall	0.63	−25.1	49.37 ± 0.19	5770 ± 30	5.67 ± 0.03

occurred since the Last Glacial Maximum low stand (~21 ka), of which as much as 75 m took place during the last 13 ka (Lambeck and Chappel, 2001; Antonioli et al., 2009; Fig. 4, upper plot). Such extreme figures are fully in range with the implied magnitude of eustatic-driven tensile deviatoric stress computed by Wallmann et al. (1988) for triggering/inhibiting dyke opening and eruption at Pantelleria. The shift in eruptive rate recorded here at ca. 13 ka occurred broadly near the midpoint of Holocene sea level rise. Fracture-sealing processes due to long-term changes in the regional stress-field are presumably threshold-controlled phenomena that become operative when enough lithostatic loading has been accommodated and distributed over the edifice. In particular, the sudden volcanic halt at 7 ka after a steady throughput at 0.8 ka^{-1} is suggestive of a threshold-controlled process culminating in complete volcanic shutdown (inside the caldera) as the sea level high stand reached its present-day value, 7–6 ka ago.

Overall, the post-20 ka intracaldera silicic system seems to have evolved at regular melt production rates, but metastably close to threshold values for mechanical failure and periodic eruption until complete lock-in at 7 ka when lithostatic-eustatic loading finally outpaced the intracaldera excess free energy needed to overcome lithostatic pressure and extract melts from progressively deeper in the magma chamber. If eustatic-volcanic processes are truly coupled at Pantelleria, the timing of volcanic shift (13 ka) and halt (7 ka) would provide two important hallmarks to constrain the critical threshold and time lag for eustatic modulation of the stress state across the magma chamber walls and the intracaldera fault network. Glacio-eustatic effects on volcanic eruptions are the focus of much ongoing work (McGuire et al., 1997; Albino et al., 2010, and references therein). Pending careful evaluation of the volumes recently erupted, the Pantelleria case may provide one of the highest-resolution $^{40}Ar/^{39}Ar$ records for quantifying such a causal link. A tectonic/fault control on intracaldera volcanism has been emphasized by previous workers (Mahood and Hildreth, 1986; Orsi et al., 1991). While we have no sufficiently extensive $^{40}Ar/^{39}Ar$ coverage to infer caldera-wide trends in spatial-temporal eruption distribution, our data do support earlier conclusions about recent focusing of the volcanic activity along the northern hingeline sector of the trapdoor structure (though this is in part a reflection of our sampling bias towards these units). The $^{40}Ar/^{39}Ar$ ages also show that considerable amounts of pantellerite magma were ponding below Mgna. Grande more recently than was previously thought, and that an active role was played by the intracaldera fracture system in draining volatile-rich magma to the South (Patite sector), or out gassed magma to the East (Mueggen sector). The implications of the newly established $^{40}Ar/^{39}Ar$ chronogram for the geochemical and petrological evolution of post-20 ka pantellerites will be explored in a forthcoming paper.

7. Summary and outlook

1 — Based on a detailed volcanostratigraphic and field survey, $^{40}Ar/^{39}Ar$ dating of post-20 ka volcanic units at Pantelleria provides a new high-resolution record of the recent post-caldera evolution. Using dedicated laser-based extraction protocols, an infra-millennial age resolution is achieved which allows isolation of the effects of excess ^{40}Ar and xenocrystic contamination that have plagued previous K–Ar studies.

2 — Radiocarbon ages determined from charcoals incorporated in (or buried by) fallout deposits are consistently younger (by up to 4 ka) than the corresponding $^{40}Ar/^{39}Ar$ age. A similar systematic bias has been documented in other equally young pyroclastic sequences, suggesting that radiocarbon data in such contexts may provide biased estimates seemingly – but insidiously – consistent with stratigraphic relationships.

3 — The new $^{40}Ar/^{39}Ar$ data capture a long-term (>15 ka) decline in eruption frequency with a shift in eruptive pace from 3.5 ka^{-1} to 0.8 ka^{-1} associated with a prominent paleosol horizon marking the only recognizable volcanic stasis between 12 and 14 ka. This shift in extraction frequency occurs without major changes in eruptive style and volume erupted, and is paralleled by a subtle trend of decreasing melt differentiation index. We speculate that this long-term decrease in frequency occurred (i) without short-term variations in melt production/differentiation rate in a steady-state compositionally-zoned silicic reservoir progressively tapped deeper through the sequence, and (ii) that it was possibly modulated by outboard eustatic forcing due to the 140 m sea level rise over the past 21 ka. Our data indicate that the intracaldera system is experiencing a protracted stasis since 7 ka. In keeping with recent geodetic evidence of deflation and subsidence of the caldera floor (De Guidi and Monaco, 2009; Mattia et al., 2007), the intracaldera system today appears to be on a wane with no temporal evidence for a forthcoming silicic eruption within 2 ka, as previously suggested.

By working at the millennial scale, our incursion into the very recent intracaldera activity of Pantelleria has produced the more precise $^{40}Ar/^{39}Ar$ dataset ever obtained on anorthoclase of such youthful age. Yet, our data indicate that it is still premature to build a time-predictive scenario of eruptions at Pantelleria based on an incomplete and potentially biased chronostratigraphic K–Ar database. High-resolution $^{40}Ar/^{39}Ar$ work focused on key units spanning the whole post-caldera activity is clearly needed to properly constrain melt productivity and eruptive rates since the GT eruption, 50 ka ago. In particular, while a possible eustatic modulation is suggested for the past 16 ka, intracaldera resurgence, trapdoor uplift, and short-term differentiation trends are all first-order processes primarily controlled by internal modifications of the magmatic system itself, independent of any surface forcing. Future $^{40}Ar/^{39}Ar$ work in this connection should address (i) the exact timing of the post-caldera trachytic volcanism, (ii) the actual time lag before the ensuing pantelleritic volcanism, and (iii) how these relate with initiation of trapdoor uplift and the time life of the present-day pantellerite reservoir. These issues bear directly on the genetic relationships between coexisting magmas in the silicic reservoir, and their short-term consequences for volcanic unrest at Pantelleria.

Supplementary materials related to this article can be found online at doi:10.1016/j.epsl.2011.07.009.

Acknowledgments

Thanks go to P. Landi (INGV, Pisa) for lending the Randazzo enclave, C. Waelbroeck (LSCE, Gif) for providing the sea level digital curve, and J.-L. Joron (LPS, Saclay) for keeping the irradiations running at Osiris. Constructive and very detailed reviews by two anonymous reviewers helped to improve the clarity of the paper. Field and lab work were supported by DPC-INGV Project Pantelleria (V3-7. 2005–2007). GVS was supported through a personnel grant from the DPC-INGV project V3-3, 2005-2007. The Ar/Ar system at the LSCE was conceived and set up by the first author as part of his CNRS integration project in this institute. This is LSCE Contribution no. 4679.

References

Albino, F., Pinel, V., Sigmundsson, F., 2010. Influence of surface load variations on eruption likelihood: application to two Icelandic sub glacial volcanoes, Grímsvötn and Katla. Geophys. J. Int. 181, 1510–1524.

Antonioli, F., Ferranti, L., Fontana, A., Amorosi, A., Bondesan, A., Braitenberg, C., Dutton, A., Fontolan, G., Furlani, S., Lambeck, K., Mastronuzzi, G., Monaco, C., Spada, G., Stocchi, P., 2009. Holocene relative sea-level changes and vertical movements along the Italian and Istrian coastlines. Quat. Int. 206, 102–133.

Avanzinelli, R., Bindi, L., Menchetti, S., Conticelli, S., 2004. Crystallisation and genesis of peralkaline magmas from Pantelleria Volcano, Italy: an integrated petrological and crystal-chemical study. Lithos 73, 41–69.

Brooks, C., Hart, S., Wendt, I., 1972. Realistic use of two-error regression treatments as applied to Rubidium–Strontium data. Rev. Geophys. Space Phys. 10, 551–577.

Chierici, R., Grassi, S., La Rosa, N., Nannini, R., Sbrana, A., Zurlo, R., 1995. Geothermal system of the Caldera of the Island of Pantelleria (Sicily Channel), in *World Geothermal Congress* — 1995. In: Berbier, E. (Ed.), World Geothermal Congress Proceedings, 19–31 may 1995, Forence, Italy, 1. Elsevier, New York, pp. 697–701.

Civetta, L., Cornette, Y., Crisci, G., Gillot, P.Y., Orsi, G., Requejo, C.S., 1984. Geology, geochronology and chemical evolution of the island of Pantelleria. Geol. Mag. 121, 541–562.

Civetta, L., Cornette, Y., Gillot, P.Y., Orsi, G., 1988. The eruptive history of Pantelleria (Sicily Channel) in the last 50 ka. Bull. Volcanol. 50, 47–57.

Civetta, L., D'Antonio, M., Orsi, G., Tilton, G.R., 1998. The geochemistry of volcanic rocks from Pantelleria Island, Sicily Channel: petrogenesis and characteristics of the mantle source region. J. Pet. 39, 1453–1491.

Cornette, Y., Crisci, G.M., Gillot, P.Y., Orsi, G., 1983. The recent volcanic history of Pantelleria: a new interpretation. In: Sheridan M.F. and Barberi F. (eds) *Explosive volcanism*. J. Volc. Geoth. Res. 17, 361–373.

de Guidi, G., Monaco, C., 2009. Late Holocene vertical deformation along the coast of Pantelleria Island (Sicily Channel, Italy). Quat. Int. 206, 158–165.

Di Carlo, I., Rotolo, S.G., Scaillet, B., Buccheri, V., Pichavant, M., 2010. Phase equilibrium constraints on pre-eruptive conditions of recent felsic explosive volcanism at Pantelleria island. Italy. J. Pet. 11, 2245–2276.

Escobar-Wolf, R.P., Diehl, J.F., Singer, B.S., Rose, W.I., 2010. $^{40}Ar/^{39}Ar$ and paleomagnetic constraints on the evolution of Volcán de Santa María. Guatemala. Geol. Soc. Am. Bull. 122, 757–771.

Esser, R.P., McIntosh, W.C., Heizler, M.T., Kyle, P.R., 1999. Excess argon in melt inclusions in zero-age anorthoclase feldspar from Mt. Erebus, Antarctica, as revealed by the $^{40}Ar/^{39}Ar$ method. Geochim. Cosmochim. Acta 61, 3789–3801.

Frey, H.M., Lange, R.A., Hall, C.M., Delgado-Granados, H., 2004. Magma eruption rates constrained by $^{40}Ar/^{39}Ar$ chronology and GIS for the Ceboruco–San Pedro volcanic field, western Mexico. Geol. Soc. Am. Bull. 116, 259–276.

Gamble, J.A., Price, R.C., Smith, I.E.M., McIntosh, W.C., Dunbar, N.W., 2003. $^{40}Ar/^{39}Ar$ geochronology of magmatic activity, magma flux and hazards at Ruapehu volcano, Taupo Volcanic Zone, New Zealand. J. Volc. Geoth. Res. 120, 271–287.

Gansecki, C.A., Mahood, G.A., McWilliams, M.O., 1996. $^{40}Ar/^{39}Ar$ geochronology of rhyolites erupted following collapse of the Yellowstone caldera, Yellowstone Plateau volcanic field: implications for crustal contamination. Earth Planet. Sci. Lett. 42, 91–107.

Giaccio, B., Marra, F., Hajdas, I., Karner, D.B., Renne, P.R., Sposato, A., 2009. $^{40}Ar/^{39}Ar$ and ^{14}C geochronology of the Albano maar deposits: implications for defining the age and eruptive style of the most recent explosive activity at Colli Albani Volcanic District, Central Italy. J. Volc. Geoth. Res. 185, 203–213.

Gioncada, A., Landi, P., 2010. The pre-eruptive volatile contents of recent basaltic and pantelleritic magmas at Pantelleria (Italy). J. Volc. Geoth. Res. 189, 191–201.

Harford, C.L., Pringle, M.S., Sparks, R.S.J., Young, S.R., 2002. The volcanic evolution of Montserrat using $^{40}Ar/^{39}Ar$ geochronology. Geol. Soc. London 21, 93–113.

Heizler, M.T., Perry, F.V., Crowe, B.M., Petres, L., Appelt, R., 1999. The age of Lathrop Wells volcanic center: an $^{40}Ar/^{39}Ar$ dating investigation. J. Geophys. Res. 104, 767–804.

Hora, J.M., Singer, B.S., Wörner, G., 2007. Volcano evolution and eruptive flux on the thick crust of the Andean Central Volcanic Zone: $^{40}Ar/^{39}Ar$ constraints from Volcán Parinacota. Chile. Geol. Soc. Am. Bull. 119, 343–362.

Jicha, B.R., Singer, B.S., 2006. Volcanic history and magmatic evolution of Seguam Island, Aleutian Island arc. Alaska. Geol. Soc. Am. Bull. 118, 805–822.

Tephrostratigraphy of silicic volcanism at Pantelleria Island, combining field observations, petrochemical data and $^{40}Ar/^{39}Ar$ dating: implications on magmatic system. PhD thesis, University of Palermo, 209 pp.

Lambeck, K., Chappel, J., 2001. Sea level change through the last Glacial Cycle. Science 292, 679–686. doi:10.1126/science.1059549.

Lowenstern, J.B., 1994. Chlorine, fluid-immiscibility, and degassing in peralkaline magmas from Pantelleria. Italy. Am. Mineral. 79, 353–369.

Lowenstern, J.B., Mahood, G.A., 1991. New data on magmatic H_2O contents of pantellerites, with implications for petrogenesis and eruptive dynamics at Pantelleria. Bull. Volc. 54, 78–83.

Mahood, G.A., Hildreth, W., 1986. Geology of the peralkaline volcano at Pantelleria, Strait of Sicily. Bull. Volc. 48, 143–172.

Mattia, M., Bonaccorso, A., Guglielmino, F., 2007. Ground deformations in the Island of Pantelleria (Italy): insights into the dynamic of the current intereruptive period. J. Geophys. Res. 112, B11406. doi:10.1029/2006JB004781.

McGuire, W.J., Howarth, R.J., Firth, C.R., Solow, A.R., Pullen, A.D., Saunders, S.J., Stewart, I. S., Vita-Finzi, C., 1997. Correlation between rate of sea-level change and frequency of explosive volcanism in the Mediterranean. Nature 389, 473–476.

Orsi, G., Ruvo, L., Scarpati, C., 1991. The recent explosive volcanism at Pantelleria. Geol. Rund. 80, 187–200.

Press, W.H., Teukolsky, S.A., Vetterling, W.T., Flannery, B.P., 1992. Numerical recipes in Fortran 77: the art of scientific computing, 1. Cambridge University Press. 933 pp. (ISBN 0-521-43064-X).

Rotolo, S.G., Villa, I.M., 2001. $^{40}Ar/^{39}Ar$ dating of an alkali-granite enclave from Pantelleria island. Per. Mineral. 70, 269–275.

Rotolo, S.G., La Felice, S., Mangalaviti, A., Landi, P., 2007. Geology and petrochemistry of recent (<25 ka) silicic volcanism at Pantelleria Island. Boll. Soc. Geol. It. 126, 191–208.

Sambridge, M.S., Compston, W., 1994. Mixture modeling of multi-component data sets with application to ion-probe zircon ages. Earth Planet. Sci. Lett. 128, 373–390.

Scaillet, S., 2000. Numerical error analysis in $^{40}Ar/^{39}Ar$ dating. Chem. Geol. 162, 269–298.

Scaillet, S., Guillou, H., 2004. A critical evaluation of young (near-zero) K–Ar ages. Earth Planet. Sci. Lett. 220, 265–275.

Scaillet, S., Vita-Scaillet, G., Guillou, H., 2008. Oldest human footprints dated by Ar/Ar. Earth Planet. Sci. Lett. 275, 320–325.

Singer, B.S., Jicha, B.R., Harper, M.A., Naranjo, J.A., Lara, L.E., Moreno-Roa, H., 2008. Eruptive history, geochronology, and magmatic evolution of the Puyehue–Cordón Caulle volcanic complex. Chile. Geol. Soc. Am. Bull. 120, 599–618.

Sircombe, K.N., 2004. AgeDisplay: an EXCEL workbook to evaluate and display univariate geochronological data using binned frequency histograms and probability density distributions. Comp. Geosci. 30, 21–31.

Spell, T.L., Smith, E.I., Sanford, A., Zanetti, K.A., 2001. Systematics of xenocrystic contamination: preservation of discrete feldspar populations at McCullough Pass Caldera revealed by $^{40}Ar/^{39}Ar$ dating. Earth Planet. Sci. Lett. 190, 153–165.

Speranza, F., Landi, P., D'Ajello, C.F., Pignatelli, A., 2010. Paleomagnetic dating of the most recent silicic eruptive activity at Pantelleria (Strait of Sicily). Bull. Volc. 72, 847–858.

Wallmann, P.C., Mahood, G.A., Pollard, D.D., 1988. Mechanical models for correlation of ring-fracture eruptions at Pantelleria, Strait of Sicily, with glacial sea-level drawdown. Bull. Volc. 50, 327–339.

Washington, H.S., 1909. The submarine eruptions of 1831 and 1891 near Pantelleria. Am. J. Sci. 27, 151–170.

Washington, H.S., 1914. The volcanoes and rocks of Pantelleria. J. Geol. 21, 653–713.

Wendt, I., Carl, C., 1991. The statistical distribution of the mean squared weighted deviation. Chem. Geol. (Iso. Geosci. Sec.) 86, 275–285.

White, J.C., Ren, M., Parker, D.F., 2005. Variation in mineralogy, temperature, and oxygen fugacity in a suite of strongly peralkaline lavas and tuffs, Pantelleria. Italy. Can. Min. 43, 1331–1347.

White, J.C., Parker, D.F., Ren, M., 2009. The origin of trachyte and pantellerite from Pantelleria, Italy: insights from major element, trace element, and thermodynamic modelling. J. Volc. Geoth. Res. 179, 33–55.